Supraglacial lake bathymetry automatically derived from ICESat-2 constraining lake depth estimates from multi-source satellite imagery

Rajashree Datta[1] and Bert Wouters[2]

[1]NASA Goddard Space Flight Center
[2]Utrecht University

November 21, 2022

Abstract

We introduce an algorithm "Watta", which automatically calculates supraglacial lake bathymmetry along tracks of the ICESat-2 laser altimeter. Watta uses photon heights estimated by the ICESat-2 ATL03 product and extracts supraglacial lake surface, bottom, corrected depth and (sub)surface ice cover on a lake. These measurements are used to constrain empirical estimates of lake depth from satellite imagery, which were thus far dependent on sparse sets of in-situ measurements for calibration. Imagery sources include Landsat OLI, Sentinel-2 and high-resolution Planet Labs PlanetScope and SkySat data, used here for the first time to calculate supraglacial lake depths. The algorithm was developed and tested using a set of 46 lakes near Sermeq Kujalleq (Jakobshavn) glacier in Western Greenland. Our results suggest that the use of multiple imagery sources (both publicly-available and commercial) in combination with altimetry-based depths, can move towards capturing the evolution of supraglacial hydrology at improved spatial and temporal scales.

Supraglacial lake bathymetry automatically derived from ICESat-2 constraining lake depth estimates from multi-source satellite imagery

R. Datta[1,2] and B.Wouters[3,4]

[1]Earth Systems Science Interdisciplinary Center, University of Maryland, College Park, MD
[2] NASA Goddard Space Flight Center, Greenbelt,MD
[3] Department of Physics, Institute for Marine and Atmospheric Research, Utrecht University, Utrecht, NL
[4] Faculty of Civil Engineering and Geosciences, Delft University of Technology, Delft, NL

Corresponding author: Rajashree Tri Datta (Tri.Datta@gmail.com)

Key Points:

- The ICESat-2 laser altimeter can detect the surface and bottom of a supraglacial lake.
- We introduce the Watta algorithm, automatically calculating lake surface, corrected bottom, (sub)surface ice at a high resolution adapting to signal strength.
- ICESat-2 depths constrain full lake depths of 46 lakes over Jakobshavn glacier using multiple sources of imagery, including very high-resolution Planet imagery

Abstract

We introduce an algorithm (*Watta*), which automatically calculates supraglacial lake bathymmetry along tracks of the ICESat-2 laser altimeter. *Watta* uses photon heights estimated by the ICESat-2 ATL03 product and extracts supraglacial lake surface, bottom, corrected depth and (sub)surface ice cover on a lake. These measurements are used to constrain empirical estimates of lake depth from satellite imagery, which were thus far dependent on sparse sets of in-situ measurements for calibration. Imagery sources include Landsat OLI, Sentinel-2 and high-resolution Planet Labs PlanetScope and SkySat data, used here for the first time to calculate supraglacial lake depths. The algorithm was developed and tested using a set of 46 lakes near Sermeq Kujalleq (Jakobshavn) glacier in Western Greenland. Our results suggest that the use of multiple imagery sources (both publicly-available and commercial) in combination with altimetry-based depths, can move towards capturing the evolution of supraglacial hydrology at improved spatial and temporal scales.

Plain Language Summary

Supraglacial lakes and streams form on the surface of Antarctica and Greenland when meltwater pools in low spots. They play an important role in the health of the ice sheets, because their water can flow to the bed of the ice sheet and lubricate the flow of the ice, or cracks may form under their weight which can cause floating ice shelves to disintegrate. In this article, we present a method that uses laser photon reflections from NASA's ICESat-2 satellites and automatically identifies lakes on the Greenland Ice Sheet and measures their depth along transects of the lake. We then use these depths to train a method that uses satellite image data of the lake to measure the depth of the entire lake. This method does not measure the depth directly, but uses the fact that the strength of reflected sunlight decreases differently at different wavelengths (green and red light) when the lake is deeper. The combination of the ICESat-2 photon measurements and the ever increasing availability of very-high resolution image data will allow us to better understand how lakes on the ice sheet evolve and affect the state of the ice sheets.

1 Introduction

Ice loss from Greenland and Antarctica is the greatest current contributor to rising sea levels, and enhanced mass loss of these ice sheets has been identified as a major tipping point after which catastrophic sea-level rise becomes irreversible (Bevis, 2019). Recent observations have shown that ice loss is accelerating faster than predicted (Slater, 2018), with a sixfold increase since the 1970/80. In Antarctica, this was largely driven by increased ocean melting of outlet glaciers (Rignot, 2019), while on the Greenland Ice Sheet mass loss is further promoted by increased surface melt and runoff (Mouginot, 2019).

Since the relationship between increasing summer air temperatures and surface melt is non-linear (Trusel, 2018), dramatic melt events have occurred in recent years in Greenland. For example, in the summer of 2019, advection of warm, wet mid-latitude air led to a summer mass loss unprecedented in the past 50 years, with widespread surface melt occurring up to the highest regions of the ice sheet (Tedesco and Fettweis, 2020; Sasgen, 2020).

While mass loss in Antarctica over the next 100 years is generally thought to be dominated by the basal melt under ice shelves (Schlegel, 2018), emerging research has focused on the potential importance of surface hydrology over Antarctica (Arthur, 2020). Supraglacial lakes have been observed around the margin of the Antarctic Ice Sheet up to high elevations (Stokes, 2019) and are likely to become more prevalent on firn-depleted ice shelves in future warming scenarios, which could potentially trigger their collapse and consequently lead to accelerated sea level rise (Lai, 2020).

On both ice sheets, meltwater pathways can include surface flow into lakes and then streams, leading to direct loss to the bed from lake drainage or the sudden termination of a stream into a moulin or near-surface flow where ice slabs can limit vertical motion (MacFerrin, 2019). The links between supraglacial hydrological systems and englacial or subglacial pathways are a complex system which can potentially be deduced by capitalizing on increasingly higher-resolution imagery and classification techniques of feature types, (Yang 2016). Past remote-sensing work has derived lake volumes from high-resolution (~1m) Worldview imagery using a physical optical depth approach as well as an empirical method using *in-situ* estimates (Moussavi, 2016; Pope, 2016). Additional work has applied a similar physically-based approach using Sentinel-2 from Copernicus (Williamson, 2018) as well as a combination of LandSat and Sentinel-2 imagery (Moussavi, 2020). The recent availability of the ICESat-2 laser altimeter since 2018 has now introduced the potential to replace the in-situ measurements used in empirical bathymetric methods with satellite laser bathymmetric depths at a high vertical resolution, consequently extracting lake volumes from imagery (Parrish, 2019). Although Sentinel-2 provides relatively high resolution (10 m) imagery with substantial coverage at a 4-day to weekly interval, usable imagery is often limited by cloud-cover, and the resolution of small streams and ice cover is imperfect. Commercial satellite imagery, which is poised to expand substantially in the future, can help fill the gap in coverage of small-scale melt and melt-induced features at a higher spatial and temporal resolution, complementing estimates resolved from Sentinel-2.

Here, we present a new algorithm, titled “Watta”, using the ICESat-2 laser altimeter to derive properties of supraglacial lakes. In addition to bathymetry (supraglacial lake depth) derived from the difference between the air-water and water-ice interface, this algorithm assigns a probability for surface type characteristics to photon returns along-track. These types include lakes, refrozen lakes, lakes with ice layers on top as well as under the surface. Additionally, we exploit a range of imagery data to validate the surface types and to derive spectrally-driven depth estimates calibrated to ICESat-2-based depths, thereby providing an estimate for meltwater volume over the full image.

The method is tested and refined using representative sections along the flowline of Sermeq Kujalleq (Jakobshavn Isbræ), one of the fastest-moving glaciers in Greenland. The repeat-tasking of imagery was designed to coincide with ICESat-2 tracks (Fig. 1), capturing lake depths at various stages of lake development during an unusually intense melt season. One of the major motivations for this tasking effort was its coincidence with several NASA Operation IceBridge (OIB) flights at the beginning and end of the summer; data from multiple instruments aboard OIB could potentially provide additional insight in future work. Over the 2019 Greenland melt season, an anomalously strong melt pulse early in the season (in June) was quickly followed by a melt pulse producing the greatest meltwater volume recorded in a single day (August 1, 2019), covering 73% of the ice sheet on July 31st, 2019 (Tedesco and Fettweis, 2020). The availability of simultaneous laser altimetry and high-resolution imagery over the season provided a rich test dataset with which to extract altimetry-based estimates of supraglacial lakes at various points in the season. ICESat-2 returns used here included strong and weak beams under various conditions. Here, we present initial results exploiting this dataset as well as introducing the *Watta* ICESat-2 surface feature detection algorithm.

[FIGURE 1]

2 Data Sources

2.1 Satellite-based Imagery and Altimetry

Our *Watta* method relies on individual photon heights as measured by ICESat-2's ATLAS instrument distributed in the ICESat-2 ATL03 product, L2A, Global Geolocated Photon Data (Neumann et al., 2019) . In addition to freely-available Landsat OLI (30m) and Sentinel-2 (10m) imagery, we incorporate very high resolution imagery from Planet Labs, including Dove-R (3m) and SkySat (~1m). Planet SkySat imagery (~1m resolution) is used to validate surface types, while all imagery sources are used to derive spectrally-driven depth estimates calibrated to ICESat-2-based depths. The high-spatial resolution of SkySat imagery allows for the identification of small-scale features on the surface and bottom of supraglacial lakes. Because SkySat imagery did not include an atmospheric correction, we compared results from Landsat, Sentinel-2 and SkySat imagery based on TOA Reflectance values. PlanetScope Dove-R data provided surface reflectance values only and is known to have issues with radiometry. However, because the method used here derives lake depth values empirically (rather than physically), this work presents the opportunity to develop accurate depth estimates using high-resolution data where calibration is imperfect, but where the data availability is high. This is particularly true for data from the PlanetScope constellation, which is frequently captured multiple times within a single day.

Because SkySat imagery did not include an atmospheric correction, Landsat, Sentinel-2 and SkySat imagery used TOA Reflectance values, whereas PlanetScope Dove-R data provided surface reflectance values only. Relative response curves for the bands used in this study are red, blue and green and NIR as shown in Fig. S1b. Finally, all imagery was coregistred with ICESat-2 using the GIMP-2 DEM.

2.2 Tasking of High-Resolution Imagery of Jakobshavn

As a part of this project, SkySat imagery was tasked for repeat cycles of ~4 days over the Greenland melt season in selected locations. Each of the 3 areas of interest presented here were approximately 600km^2 on average. Repeat imagery was specifically chosen to cover flowlines of fast-flowing glaciers, including Sermeq Kujalleq, as in this study (Fig. 1). In addition, repeat tracks were designed to coincide with both (a) overpasses of the recently-launched NASA ICESat-2 laser altimeter and, (b) several flights of the airborne NASA Operation IceBridge mission in the beginning and end of the season. Here, we present the first work exploiting this stacked dataset for method development, restricted to available satellite imagery/altimetry.

The final set of lakes used for the development of the ATL03-based method included 50 lakes (46 discussed here), 14 of which coincided with very high-resolution imagery (SkySat).

3 Methods

Watta is an algorithm which accepts ICESat-2 ATL03 as input and automatically detects supraglacial surface features with an associated probability of likelihood. In its current state, the algorithm detects only lakes and their associated surface, lake bottom and corrected depth estimate as well as subsurface ice when present (Fig. 2 left). A subsequent set of steps processes imagery from SkySat, PlanetScope, Sentinel-2 and Landsat OLI to produce a delineation of the lake boundary based on the normalized difference water index (NDWI), where we standardized the index (setting all values between 0 and 1 from minimum to maximum) due to negative NDWI values produced from PlanetScope data. Next, an empirical relationship for each selected band between the depth estimate calculated by *Watta* and the coregistered imagery pixels and finally, and a final depth estimate for the entire lake based on this empirical relationship for a chosen band. The empirical relationship is based on the exponential decay of reflectance at water depth, as detailed by Box and Ski (2007), where, given coincident corrected depth values as calculated by *Watta* (D) and reflectance values from imagery (R), we estimate the α-coefficients in eq. 1, which can then be applied to calculate water depth over the full-scale of imagery where lakes are delineated.

$$D = \alpha_0 / (R + \alpha_1) + \alpha_2 \qquad \text{(eq. 1)}$$

The codebase for *Watta* (Fig. 2 left) is divided into a module defining surface and bottom returns ("Surface Detection") at the native resolution of ICESat-2, and an "Interpretive" layer that resolves the bottom/surface combination to specific supraglacial features, in this case lakes. Surface detection determines, for a collection of 75 photons surrounding any individual photon (Step a), the first three peak probabilities for height within in a kernel density, estimating a mean height for the surface (or top of a lake or refrozen pond), the main bin directly below the surface, a surface bottom and a potential third peak (potentially subsurface ice), where photons are selected without regard to confidence level. We confirm that the bottom estimate is robust, i.e. detected when the density estimate uses a bin value of 0.1m as well as with 0.3m (Step b). Where outliers are found in Step c, the kernel density estimate is recalculated with a larger number of photons (in multiples of 75), and where these values continue to be outliers, they are removed (for later interpolation). Finally, we apply a simple correction for refraction, described in Parrish et al. (2019), noting that no data used in this study was collected when ICESat-2 pointed off-nadir (which could affect the equation).

[FIGURE 2]

The interpretive layer first performs more sophisticated smoothing (Step d), removing estimates for top and bottom values which more closely resemble the background rate (as determined from a local 5000 photon-count window). The top surface is then divided into segments based on breaks in the surface slope, and lakes are detected using a classification scheme taking into account the local surface slope and the strength of the bottom return (Fig.2 bottom). For example, a segment with a surface slope smaller than 0.03% and a strong double peak in the histogram of that segment's photon heights is given a lake classification of 'highly likely', whereas segments passing the same slope threshold but not showing showing a bottom return are identified as 'likely ice-covered' lakes. On the other hand, segments with a slope exceeding 0.3% and no significant peak below the surface in the histogram are allocated to the 'highly unlikely' lake class. (Step e). Where lakes are detected, we then perform a higher resolution recalculation of the kernel density estimate, limiting the calculation to values below the surface and only 30 photons (Step f). The edges of the lake are then reset to recategorize values interpreted as an ice layer near the ends and seal the bottom of the lake to the top (Step g). The final step of the algorithm creates outputs which (Step h) assign physical meaning to each photon (e.g. lake surface, bottom, corrected depth, surface ice, subsurface ice). The resulting bottom photons are passed through an iterative robust quadratic local regression (rloess) filter, where remaining outliers are removed when deviating substantially from the smoothed bottom estimate.

In order to develop imagery-based depths, we primarily use the computer vision toolbox in Matlab, except for the coregistration of imagery. We align imagery with ICESat-2 returns (Step j) by standardizing all imagery to the nearest Landsat image, using the arosics library in Python (Scheffler et al., 2017). Coregistration between ICESat-2 photon locations and imagery is managed by registering ICEsat-2 with the GIMP-2 DEM (used for georeferencing of Landsat), by transforming the point cloud using the iterative closest point algorithm. ICESat-2 mission requirements list a geolocation accuracy of 6.5m (Neuenschwander, 2019), thus to calculate imagery values associated with an ICESat-2 photon, we calculate overlapping imagery 6m in each direction perpendicular to the beam and calculate a mean. We use a standard NDWI (with the green and NIR) bands to deliberately include regions with ice layers, rather than the modified $NDWI_{ice}$,, per Yang and Smith, (2013) calculated from the coregistered imagery to determine the boundaries of lakes (Step l), using adaptive thresholding (Bradley et al., 2007) to generate a binary mask and then determine the boundaries of individual lakes. We note that the height of the lake surface for any imagery source is calculated based on the elevation where the lake edge intersects with the corrected bottom surface, as calculated by *Watta*.We then provide the coregisted ICESat-2 depths and red or green bands from imagery to develop an empirical relationship (Step k), finally applying the relationship to the full lake.

4 Results

4.1 Physical constraints of the test dataset

The test dataset provides a diversity of lake types, with the largest surface area calculated at 5.6 km^2 and a maximum *Watta*-calculated corrected depth at 10.3 m; a number of lakes contain substantial ice cover. Lake Amitav was selected for closer examination because despite the dense photon cloud, its depth, length and variability and the presence of ice cover pose a challenge for our detection algorithm, and because of the availability of multiple imagery sources. Lake Martha is chosen because it represents an ideal case for the algorithm, while Lake Zadie is chosen because two beams passed over the same lake with SkySat imagery available one day afterwards. A basic assumption we make in this study is that the lake bottom remains relatively consistent over several days, although past research on 2 lakes in Western Greenland has estimated lake bottom ablation rates at 6.5 cm/day on the bottom of the pond (Tedesco et al., 2012). We assume that this is the primary physical source of uncertainty in the empirical calculation, as the relationship will degrade with temporal distance from the ICESat-2 pass. However, where changes in the bathymetry are not uniform, we can potentially make inferences about drainage mechanisms (e.g. the forming and deepening of crevasses). Cross-sections showing the lake top, bottom, and bottom value corrected for refraction as calculated by *Watta* along with lake top and bottom as calculated empirically from imagery, are shown in Supplemental Fig. S4, Table S1.

4.2 Evaluating *Watta*

The most rigorous weighting system used for the algorithm, using only lake classes 1,2,4 and 7, succeeded in automatically detecting 49 out of the 50 lakes identified in the available imagery, with two likely false positives (i.e. not confirmed by NDWI values exceeding 0.2 in the imagery) . A less rigorous weighting system, including lake class 3, detected the 50th lake,but resulted in a large number of false positives in areas of steep, and rough topography, where abrupt changes in the photons elevations are misinterpreted as bottom reflections by the algorithm.

In the absence of simultaneous in situ data, we evaluate the performance of the algorithm based on visual inspection. Additionally, where an empirical relationship with imagery is successful (a high correlation coefficient value), we take this as this partial evidence that ICESat-2 and imagery sources have detected bathymetry correctly. The most successful bottom retrieval occurred where ice cover was minimal, the density of photons was high and where the bottom slope was relatively uniform (e.g. Lake Martha). The presence of ice near the surface (between the surface and 1m below the surface) frequently obscured lake bottom detection (e.g. reference ground track (RGT) 1222, Lake 3 in Fig. S4), although in some cases only partially; however, the presence of subsurface ice did not immediately preclude the presence of a strong bottom return (e.g. Lake 7, RGT 1169, Fig. S4). The algorithm therefore indicates the presence of surface/near-surface ice, but does not automate the removal of the calculated bottom return. We can confirm the presence of an ice layer both by visual inspection of the imagery and by comparing standardized NDWI values calculated from imagery coincident with the ICESat-2 track (Fig S1a). We note that for at least one case, (RGT 1108 Lake 6, Fig. S4), the designation of "lake" was ambiguous, as this could be treated as either a shallow lake containing a large amount of subsurface ice, or as a slush layer (a number of which were identified elsewhere).

4.2 Evaluating Data Sources for Imagery-based Depth Calculations

Total uncertainty for the empirically-based depth estimate from imagery is comprised of uncertainty in ICESat-2 geolocation, uncertainty from the *Watta* algorithm itself (which operates at a vertical resolution of 0.3m), from the resolution of the imagery and finally from physical changes in the lake occurring between the time that imagery is captured and the ICESat-2 pass. Comparisons are considered more valuable when the lake surface calculated by imagery vs altimetry differ by less than a meter (and are preferably estimated for the same day); here we estimate accuracy with a simple R^2 value.

Past work has considered either the red or green band for depth estimates (Moussavi et al., 2020; Williamson et al., 2018) but we note that available in situ validation was limited at the time (Pope et al., 2016). For Landsat, Sentinel and SkySat, the empirical depth estimates for the red band showed slightly-higher fidelity in shallow water, whereas for deeper water the green-band estimates outperforms the red band when compared to the ICESat-2 based Watta estimates, in agreement with Moussavi et al. (2016). We note that the green band is able to resolve bathymetry at greater depths and tends to emphasize cracks at the bottom of the lakes, as shown over Lake Martha (Fig 3a). The major exception was PlanetScope data, where the red band consistently showed greater fidelity to ICESat-2-based estimates while green band estimates produced unrealistic depth estimates. We note that because this method is empirical, future users would be able to select bands or combinations, as with the average of the panchromatic and red band used by Pope et al. (2016), that provide the greatest fidelity to ICESat-2 based observations. However, a thorough comparison is outside of the scope of this initial study.

To demonstrate the robustness of the Watta algorithm as well as the impact of band choice, we show depths calculated from two beams passing over Lake Zadie on June 13th, followed by retrieval of SkySat imagery on June 14th and Sentinel-2 on June 16th (Fig. 3 b,c and RGT 1222 Lake 5(6) in Supplemental Profiles). The green band shows higher R^2 values for both Sentinel-2 and SkySat for 3 of 4 cases (excepting SkySat 3r). Depths calculated from the 3l beam are slightly larger and red-band based maximum depths are greater, whereas a finer bathymmetric relief is captured by the green band in both SkySat and Sentinel-based depth estimates (Fig. 3d, box). We note that even when high R^2 values are calculated between the empirical estimate and Watta-calculated depths, unrealistic depths can result when lake drain or fill rapidly, and low-resolution imagery can potentially resolve the height of a lake surface inaccurately (Fig. S2).

[FIGURE 3]

Within Figure 4, we show the depth evolution of Lake Amitav over 5 days, both along the ICESat-2 ATL03/*Watta*-calculated profile and for the full image using the empirical equation. Rising lake levels are demonstrated both by the expansion of the lake through time (right column) and the rise in the lake level (cyan line, left column). Planet SkySat estimates at a 1m resolution (Fig. 4c) shows the greatest level of detail of crevassing at the bottom of the lake although PlanetScope estimates, at a 3m resolution (Fig. 4f,g) are comparable. We note that PlanetScope data showed variations in the fidelity to *Watta*-based estimates between the green band vs the red band. However, the bottom relief is maintained at depth with PlanetScope, and it would be possible to calibrate values to Sentinel estimates, which may result in more reliable estimates while still providing very high-resolution depth estimates.

[FIGURE 4]

5 Conclusions

This study represents initial work developing the *Watta* algorithm for lake depth estimates as well as subsurface ice detection, with a unique stacked dataset over Western Greenland during an intense melt season. We demonstrate the potential of ICESat-2 for automated lake detection and depth estimation, and how empirically-derived depths derived from a combination of imagery sources can complement strengths and weaknesses, e.g. the geolocational accuracy and historical record provided by Landsat (despite low spatial resolution) versus the high spatial and temporal resolution provided by Planet Labs PlanetScope data (despite radiometric and geolocation issues). Together, such a time series can provide valuable information about the evolution of ice cover and drainage mechanisms as well as volume estimates. We note that given the accelerating sophistication of altimetry-based observations, ongoing efforts to improve geolocation, radiometric quality or frequency in high-resolution imagery are crucial, and the availability of simultaneous imagery and altimetry would enhance the capabilities of other satellite imagery sources to fill out the time series by providing a calibration standard.

Our algorithm successfully detects a wide variety of lake types automatically, and can be applied to the growing set of ICESat-2 and imagery data over large sections of Antarctica and

Greenland. Identification of narrow stream features on sloping surfaces, however, still needs visual verification due to the large number of false positives. This will be addressed in future work, together with adding features to the interpretive layer, including slush layers as well as cracks, using the Planet SkySat imagery dataset for testing purposes.

Acknowledgments, Samples, and Data

B.W. was funded by NWO VIDI grant 016.Vidi.171.063. R.T.D. was funded by the ICESat-2 Project Science Office.

Final imagery/Watta-based depth calculations are available at https://doi.org/10.5281/zenodo.4067629

References

Arthur, J. F., et al. (2020). Distribution and seasonal evolution of supraglacial lakes on Shackleton Ice Shelf, East Antarctica. *The Cryosphere Discussions*, *2020*, 1–36. https://doi.org/10.5194/tc-2020-101

Barsi, J. et al.. (2014). The Spectral Response of the Landsat-8 Operational Land Imager. *Remote Sensing*, *6*(10), 10232–10251. https://doi.org/10.3390/rs61010232

Bradley, D., & Roth, G. (2007). Adaptive Thresholding using the Integral Image. *Journal of Graphics Tools*, *12*(2), 13–21. https://doi.org/10.1080/2151237X.2007.10129236

Lai, C.-Y., et al. (2020). Vulnerability of Antarctica's ice shelves to meltwater-driven fracture. *Nature*, *584*(7822), 574–578. https://doi.org/10.1038/s41586-020-2627-8

MacFerrin, M., et al. (2019). Rapid expansion of Greenland's low-permeability ice slabs. *Nature*, *573*(7774), 403–407. https://doi.org/10.1038/s41586-019-1550-3

Mouginot, J., et al. (2019). Forty-six years of Greenland Ice Sheet mass balance from 1972 to 2018. *Proceedings of the National Academy of Sciences*, *116*(19), 9239. https://doi.org/10.1073/pnas.1904242116

Moussavi, M. et al. (2020). Antarctic Supraglacial Lake Detection Using Landsat 8 and Sentinel-2 Imagery: Towards Continental Generation of Lake Volumes. *Remote Sensing*, *12*(1), 134. https://doi.org/10.3390/rs12010134

Neuenschwander AL, Magruder LA.(2019). Canopy and Terrain Height Retrievals with ICESat-2: A First Look. *Remote Sensing*. *11*(14):1721. https://doi.org/10.3390/rs11141721

Neumann, T. A. et al. (2019). The Ice, Cloud, and Land Elevation Satellite – 2 mission: A global geolocated photon product derived from the Advanced Topographic Laser Altimeter System. *Remote Sensing of Environment*, *233*, 111325. https://doi.org/10.1016/j.rse.2019.111325

Parrish, C. E. et al. (2019). Validation of ICESat-2 ATLAS Bathymetry and Analysis of ATLAS's Bathymetric Mapping Performance. *Remote Sensing*, *11*(14), 1634. https://doi.org/10.3390/rs11141634

Pope, A. et al. (2016). Estimating supraglacial lake depth in West Greenland using Landsat 8 and comparison with other multispectral methods. *The Cryosphere*, *10*(1), 15–27. https://doi.org/10.5194/tc-10-15-2016

Rignot, E. et al. (2019). Four decades of Antarctic Ice Sheet mass balance from 1979–2017. *Proceedings of the National Academy of Sciences*, *116*(4), 1095–1103. https://doi.org/10.1073/pnas.1812883116

Sasgen, I. et al. (2020). Return to rapid ice loss in Greenland and record loss in 2019 detected by the GRACE-FO satellites. *Communications Earth & Environment*, *1*(1), 8. https://doi.org/10.1038/s43247-020-0010-1

Scheffler, D. et al (2017) : An Automated and Robust Open-Source Image Co-Registration Software for Multi-Sensor Satellite Data. *Remote Sensing*,9(7),676. https://doi.org/10.3390/rs9070676

Schlegel, N.-J. et al. (2018). Exploration of Antarctic Ice Sheet 100-year contribution to sea level rise and associated model uncertainties using the ISSM framework. *The Cryosphere*, *12*(11), 3511–3534. https://doi.org/10.5194/tc-12-3511-2018

Slater, T. et al. (2020). Ice-sheet losses track high-end sea-level rise projections. *Nature Climate Change*, *10*(10), 879–881. https://doi.org/10.1038/s41558-020-0893-y

Stokes, C. R. et al. (2019). Widespread distribution of supraglacial lakes around the margin of the East Antarctic Ice Sheet. *Scientific Reports*, *9*(1), 13823. https://doi.org/10.1038/s41598-019-50343-5

Tedesco, M. et al. (2012). Measurement and modeling of ablation of the bottom of supraglacial lakes in western Greenland. *Geophysical Research Letters*, *39*(2). https://doi.org/10.1029/2011GL049882

Tedesco, M., & Fettweis, X. (2020). Unprecedented atmospheric conditions (1948–2019) drive the 2019 exceptional melting season over the Greenland ice sheet. *The Cryosphere*, *14*(4), 1209–1223. https://doi.org/10.5194/tc-14-1209-2020

Williamson, A. G. et al. (2018). Dual-satellite (Sentinel-2 and Landsat 8) remote sensing of supraglacial lakes in Greenland. *The Cryosphere*, *12*(9), 3045–3065. https://doi.org/10.5194/tc-12-3045-2018

Yang, K. & Smith, L. C. (2013). Supraglacial Streams on the Greenland Ice Sheet Delineated From Combined Spectral–Shape Information in High-Resolution Satellite Imagery. *IEEE*

Geoscience and Remote Sensing Letters, *10*(4), 801–805. https://doi.org/10.1109/LGRS.2012.2224316

Yang, K., L. et al. (2017). Automated High-Resolution Satellite Image Registration Using Supraglacial Rivers on the Greenland Ice Sheet. *IEEE Journal of Selected Topics in Applied Earth Observations and Remote Sensing*, *10*(3), 845–856. https://doi.org/10.1109/JSTARS.2016.2617822

Figure 1. Study region over Sermeq Kujalleq. Left: Lake Amitav (a) Planet SkySat visual (b) Cross section, calculated by *Watta* (c) Repeat-tasking locations for Planet SkySat shown in white boxes over annual velocity estimates from MEaSUREs (NSIDC). Center track,ICESat-2 repeat ground tracks shown in green. Three lakes used throughout text and figures include Lake Amitav, Lake Martha and Lake Zadie.

Figure 2. Diagram of main methods, described in main text. *Watta* weighting scheme for lakes (i) is detailed in bottom table

Figure 3. *Watta*-calculated and imagery-derived depths. Lake Martha (a), Lake Zadie: Sentine-2l (l,m), Planet SkySat (n,o). *Watta*/imagery-derived derived depths over Lake Zadie with both beam 3r and 3l: (b,c): False-color imagery and ICESat-2. (d-k) Depths from imagery source, band/beam as shown

Figure 4. Lake Amitav, filling over five days between May 20th and May 25th, with ICESat-2 pass on May 23rd. Left column: Profiles with Watta-calculated and imagery-derived depths from the green and red bands (with corresponding R^2 values inset), legend same as Fig.3a. Right column: Depth values derived from empirical estimate, with imagery source , date collected, band used for depth estimate shown

Supplemental Tables and Figures.

Lakes Over Sermeq Kujalleq

Designation	**Max Lake Surface Area from imagery (m^2)**	**ICESat-2 track length (m)**
RGT 727 May 15th, 2019		
1	160800	2754.44
RGT 841 May 23rd		
1	357900	2398.82
2	880300	3092.19
3	804873	2786.51
4	880300	3372.80
5	625127	2608.30
RGT 1108 June 9th, 2019		
1	574200	3350.97
2	574200	3123.05
3	596931	3026.49
4	956190	3360.29
5	772089	2746.55
6	54167	2665.72
7	987300	3165.52
8	738000	3172.79
9	1165500	2691.53
10	987300	2968.48
11	738000	3228.69
RGT 1169 June 13th, 2019		
1	158400	2885.59
2	513200	2455.54
3	224100	2396.62
4	478100	3307.89
5	904600	2817.40
6	904600	2720.19
7	1113500	3698.78
8	1113500	2401.77
9	1113500	2612.26
RGT 1222 June 17th, 2019		
1	2060100	3134.91
2	48600	2618.15
3	1635300	4089.09
4	255600	2718.01

5	1635300	4129.21
6	1692900	2679.53
7	2225700	3181.78
8	1611900	4443.29
9	998574	2541.70
10	998574	2802.32
11	1025100	3193.46
12	1611900	4210.25
13	1025100	3860.27
14	4101300	4774.88
15	2060100	3842.27
16	998574	2562.81
17	4101300	4602.40
18	5656500	4005.92
19	2982600	2899.97

Table 1: Lakes used in this study with maximum surface area of the lake detected from imagery and the length of the ICESat-2 pass over the lake. Lake numbers correspond to profiles shown in Supplemental Figure 3.

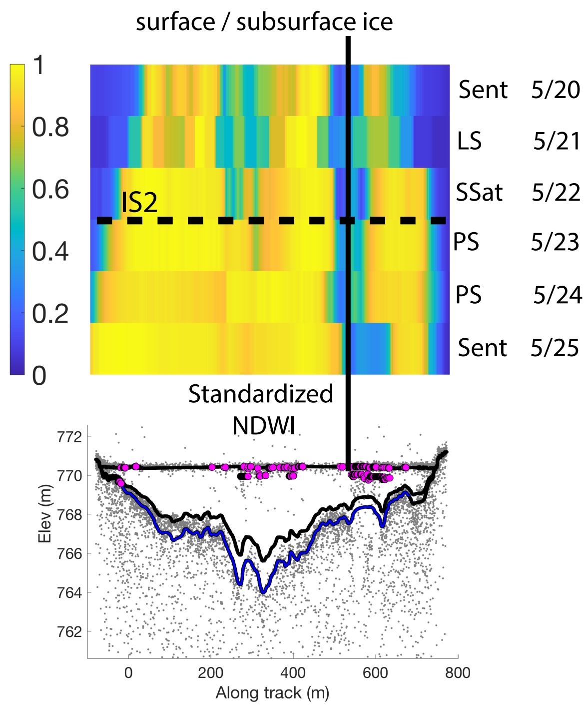

(a) Lake Amitav NDWI

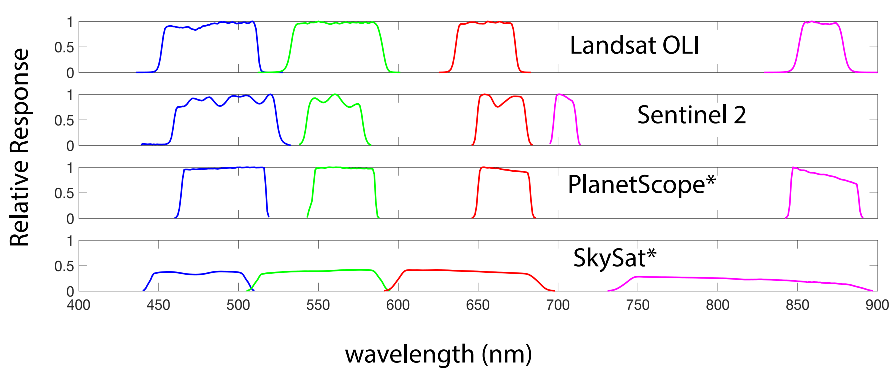

(b) Spectral Response

Figure 1: (a) Watta calculated profile of depth, depth corrected for refraction and subsurface ice over Lake Amitav (bottom) with NDWI values co-registered to the ICESat-2 track (top) (b) Spectral Response curve for imagery sources used in main text. Note that PlanetScope and SkySat data are shown for the satellite used in imagery collected over Lake Amitav and are not representative of the entire constellation. Landsat OLI source (Barsi et al., 2014)., Sentinel-2 source (https://earth.esa.int/web/sentinel/user-guides/sentinel-2-msi), Planet Labs SkySat and PlanetScope (see: support.planet.com)

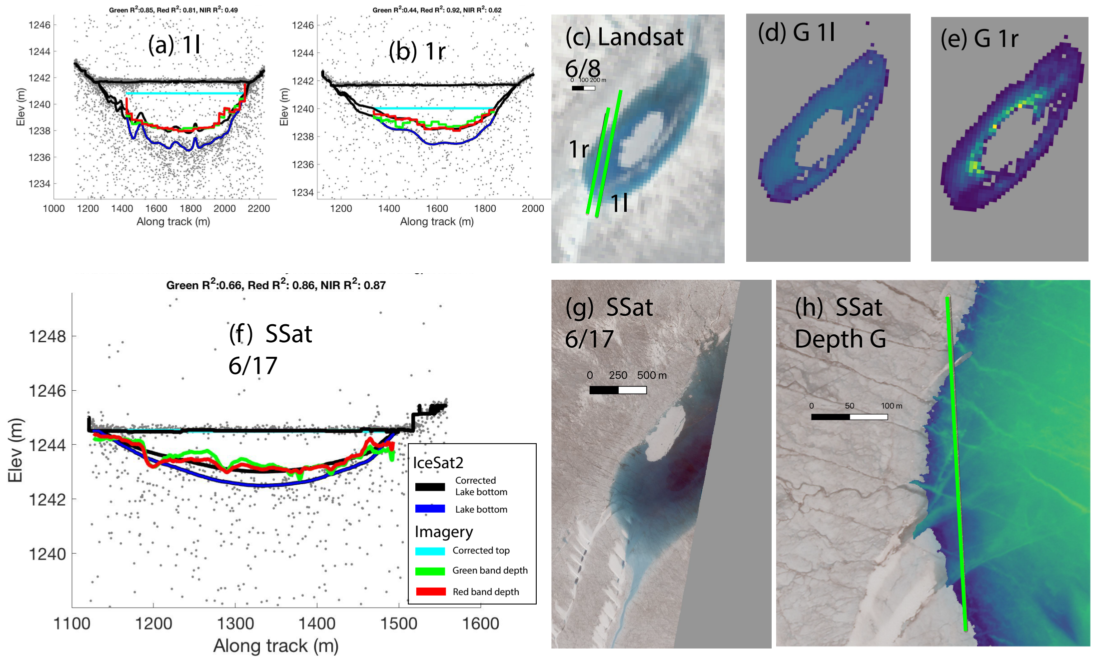

Figure S2: Watta-calculated depth, corrected depth and lake surface profiles for (top) RGT 1108 Lake 1 on June 9th, 2019, with gt1l (a,d) and gt1r (b,e). Landsat imagery collected on June 8th, 2019. (bottom) The same lake, also RGT 1222 Lake 6 on June 17th, 2019 (f-h), with SkySat imagery collected on June 17th, 2019.

Figure: S3. Lake Depth Profiles (corresponding to Table S1)

RGT 727 May 15th, 2019

Lake 1:

Sentinel-2: May 12th, 2019

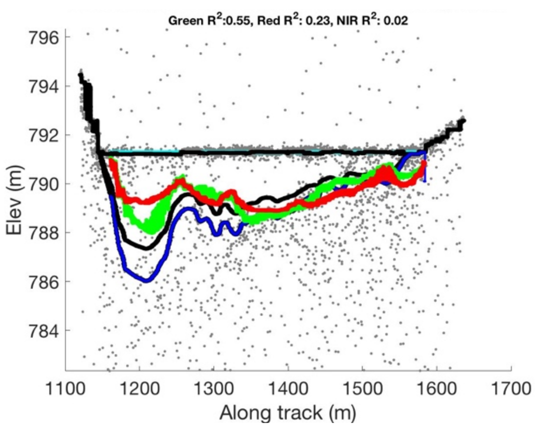

Sentinel-2: May 14th, 2019

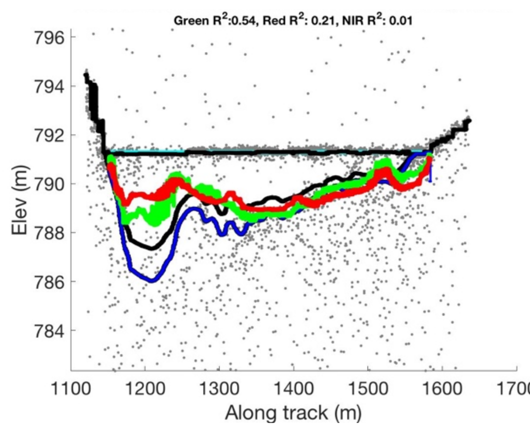

RGT 841 **May 23rd, 2019**

Lake 1

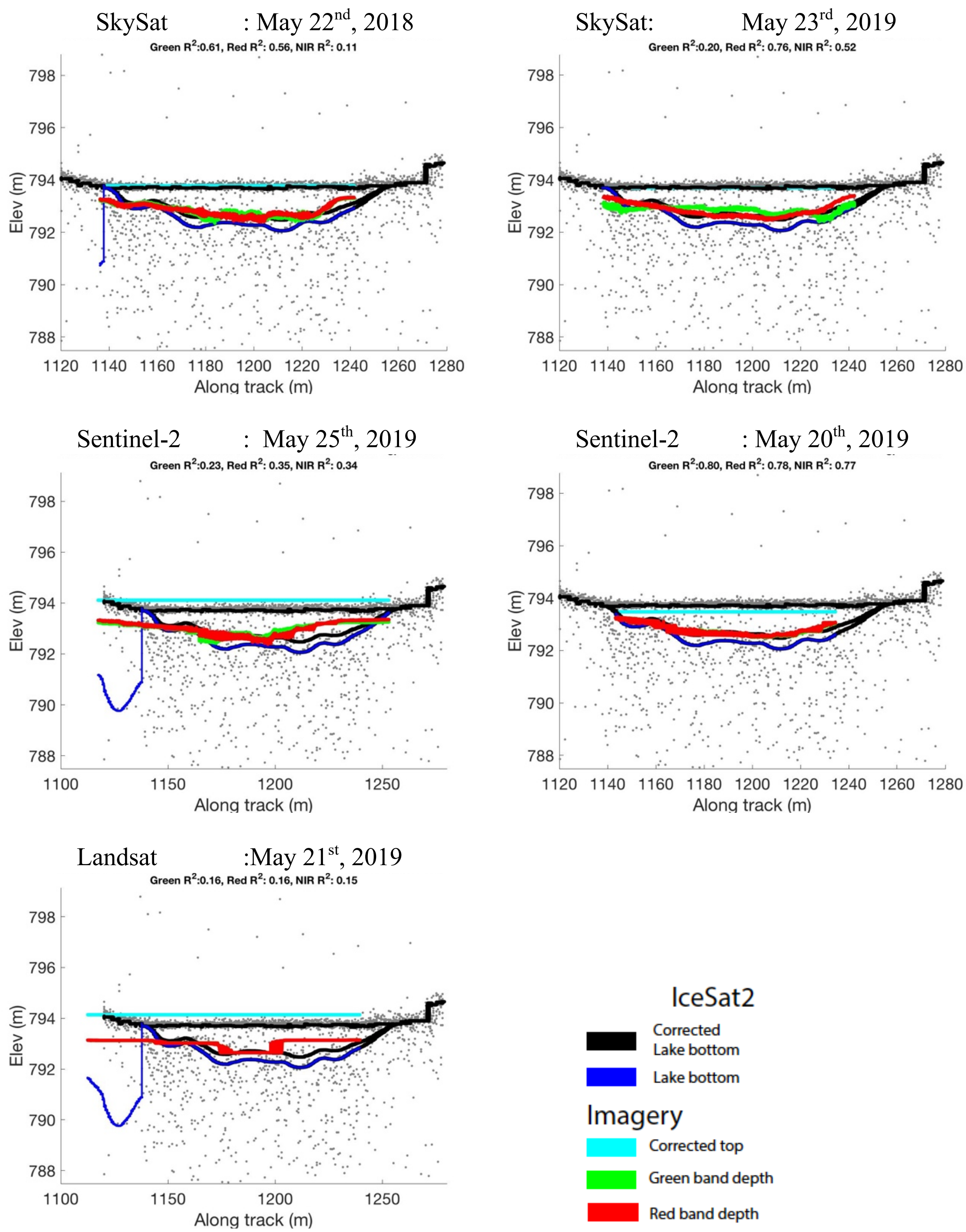

Lake 2:

SkySat: May 22nd

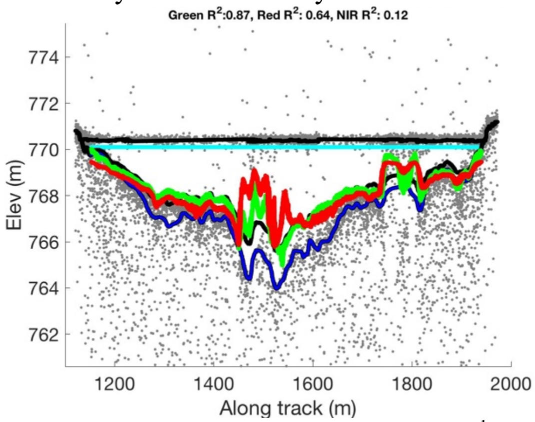

PlanetScope: May 24th

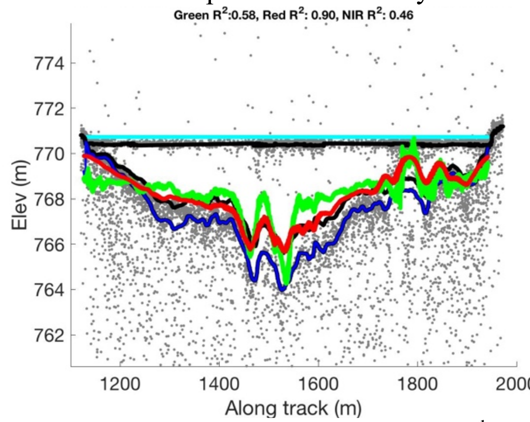

PlanetScope :May 23rd

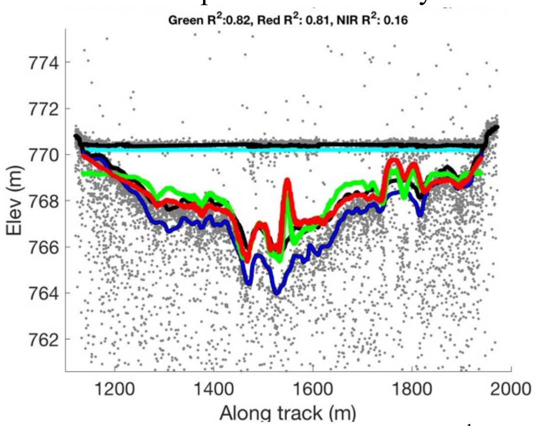

Sentinel-2 :May 25th

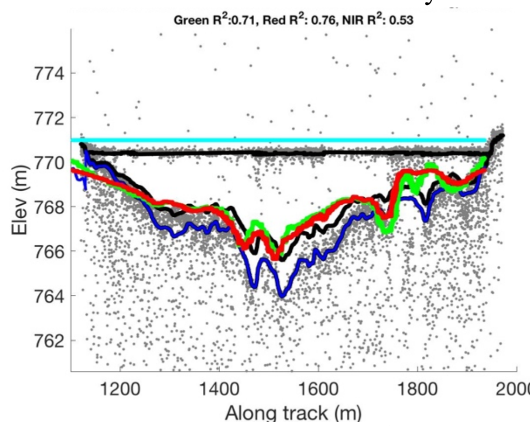

Sentinel-2 May 20th

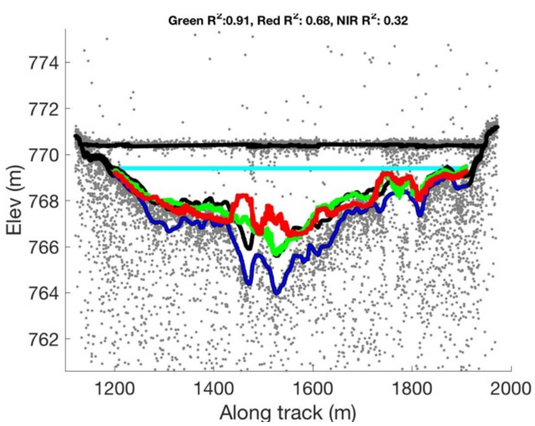

Landsat :May 21st

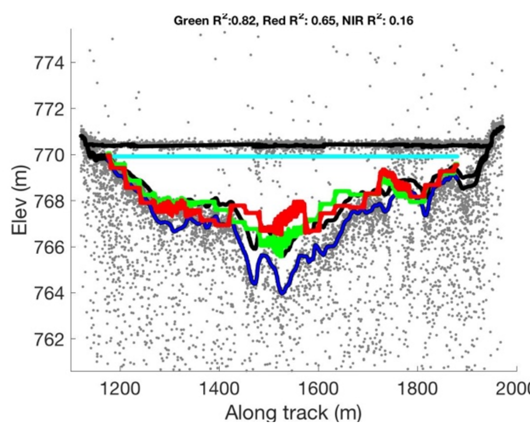

RGT 841 May 23rd, 2019

Lake 3:

SkySat: May 22nd

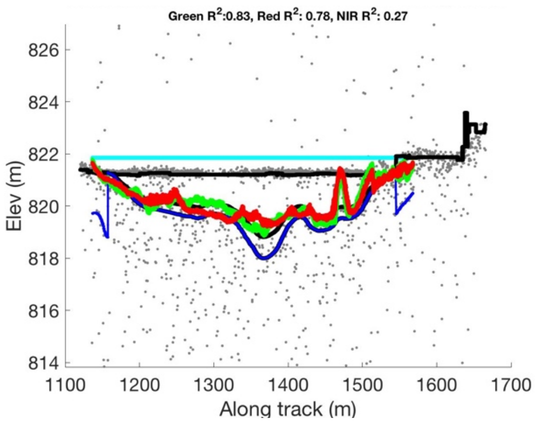

Sentinel-2 May 25th

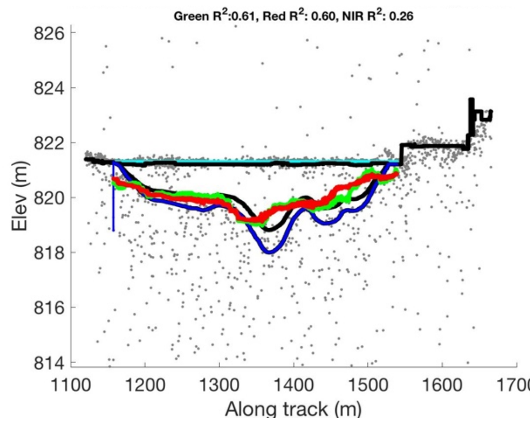

Sentinel-2 May 20th

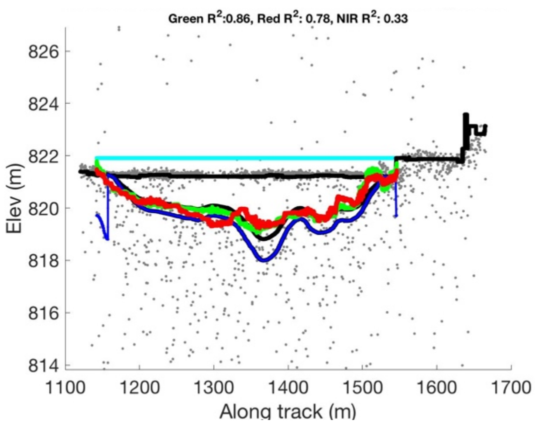

Landsat May 21st

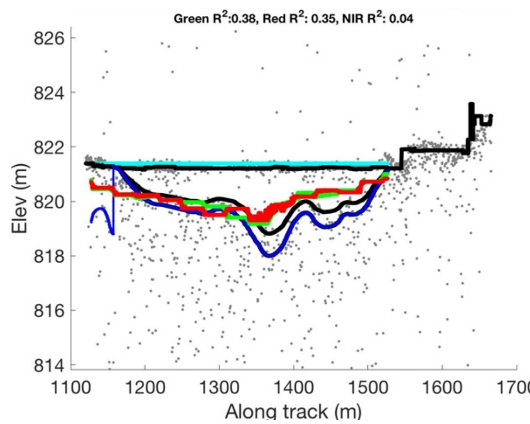

RGT 841 **May 23rd, 2019**

Lake 4:

SkySat :May 22nd

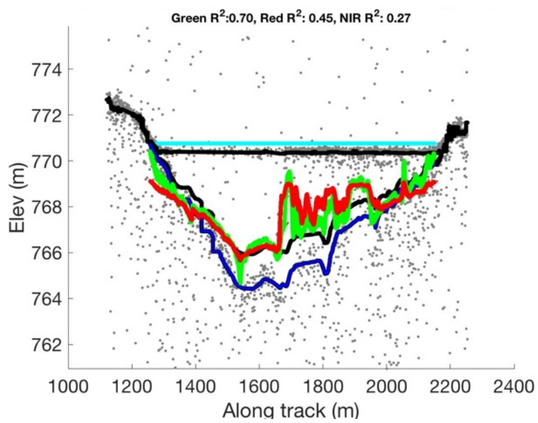

PlanetScope :May 24th

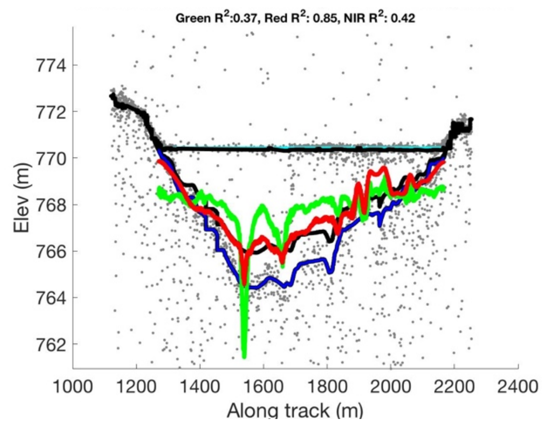

PlanetScope :May 23rd

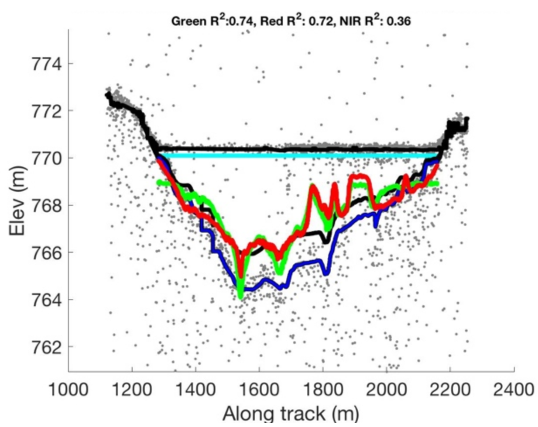

Sentinel-2 May 25th

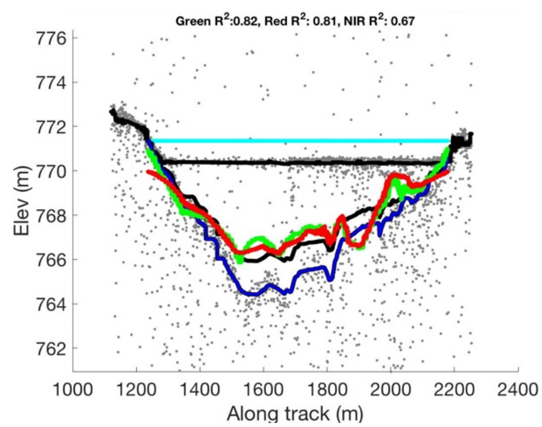

s

Sentinel-2 May 20th

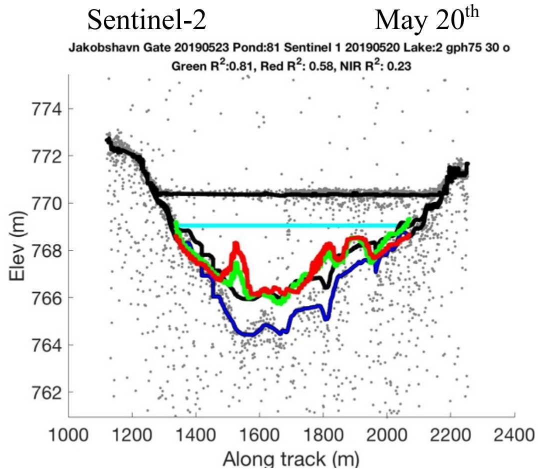

Landsat May 21st

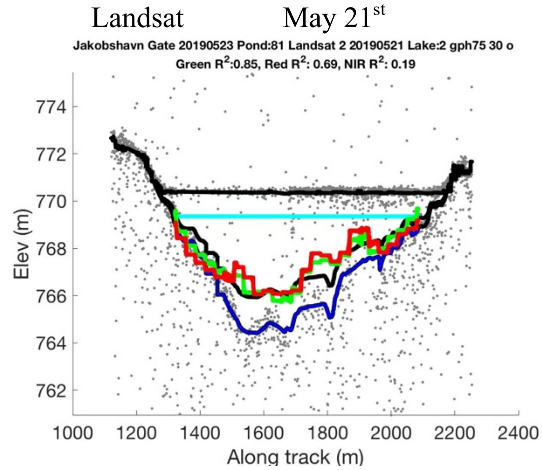

RGT 841 May 23rd, 2019

Lake 5:

SkySat :May 22nd

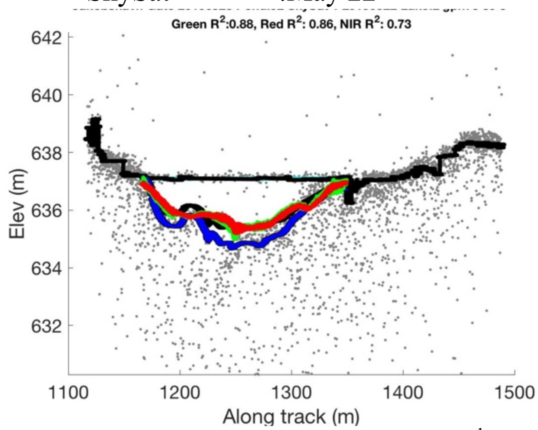

PlanetScope :May 24th

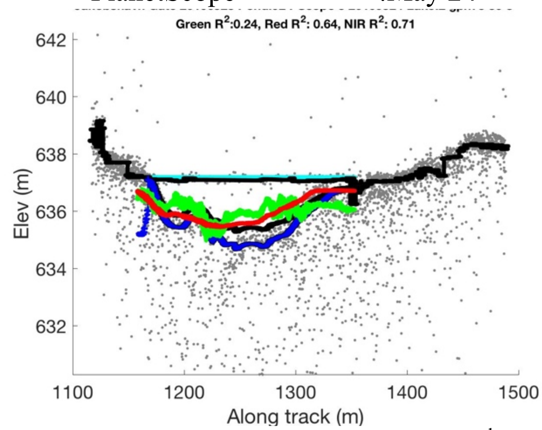

PlanetScope :May 24th

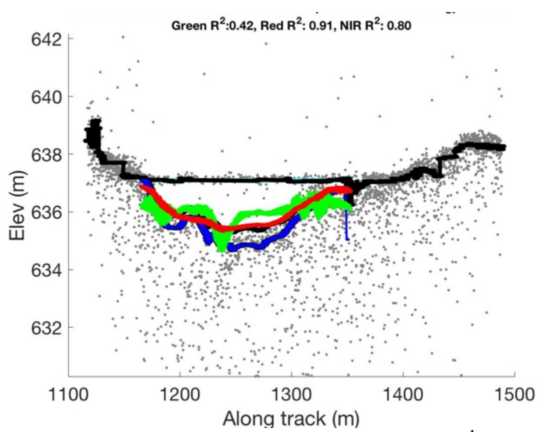

PlanetScope :May 23rd

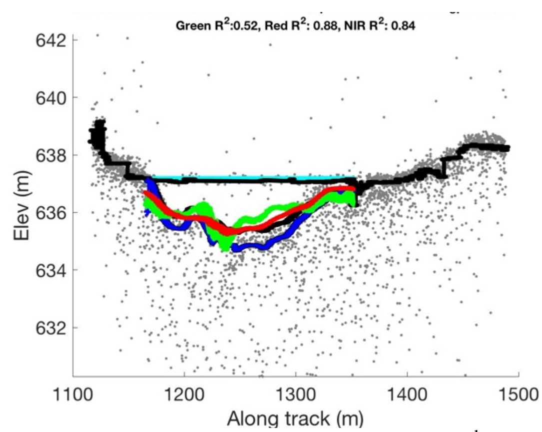

Sentinel-2 May 25th

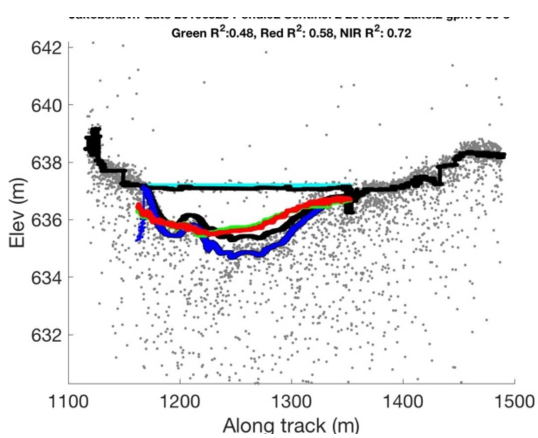

Sentinel-2 May 20th

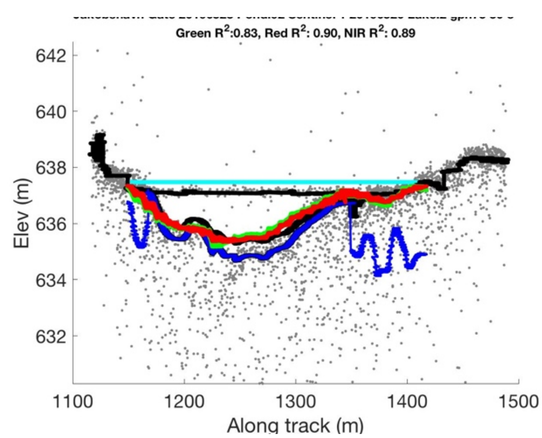

Lake 5 cont…

Landsat May 23rd

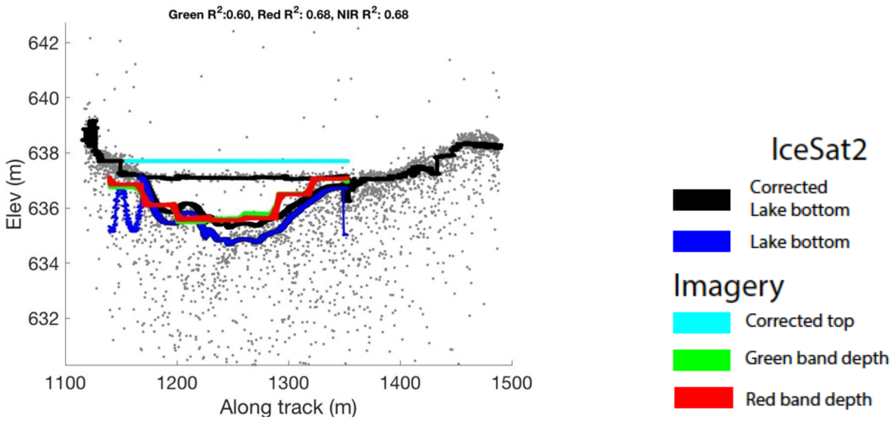

RGT 1108 June 9th, 2019

Lake 1

Landsat June 8th

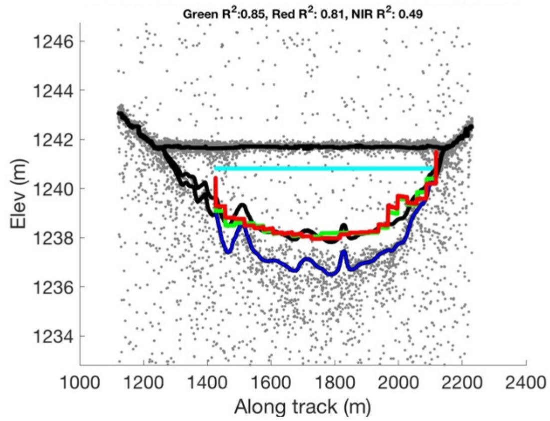

Lake 2:

Landsat June 8th

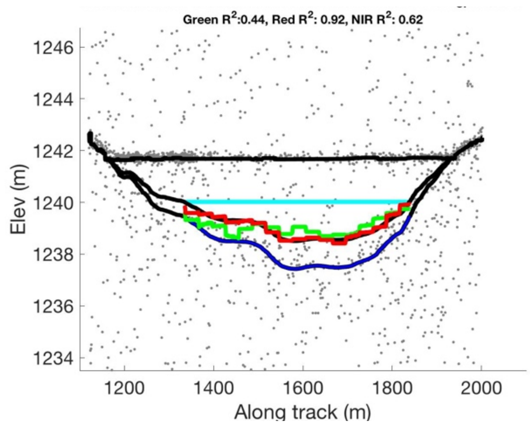

Lake 3:

Landsat June 8th SkySat June 8th

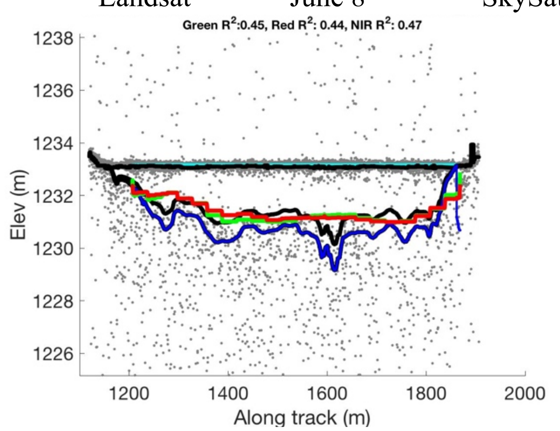

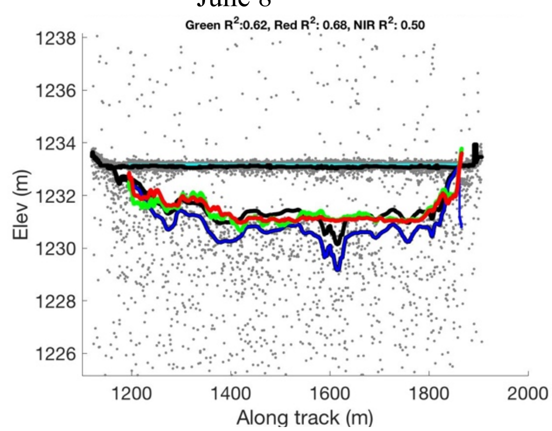

RGT 1108 **June 9th, 2019**

Lake 4

Landsat June 8th SkySat June 8th

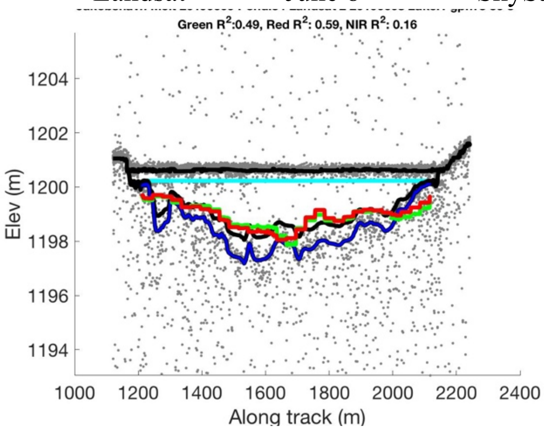

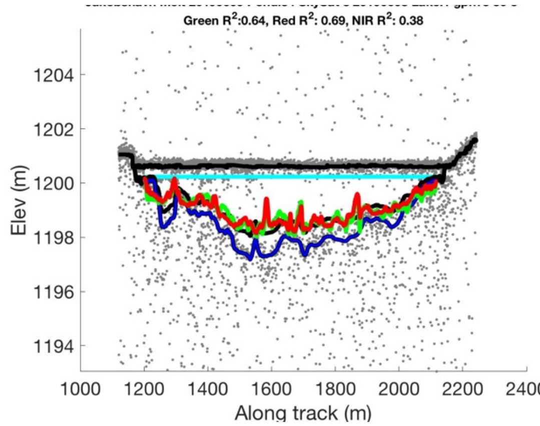

Lake 5

Landsat June 8th SkySat June 8th

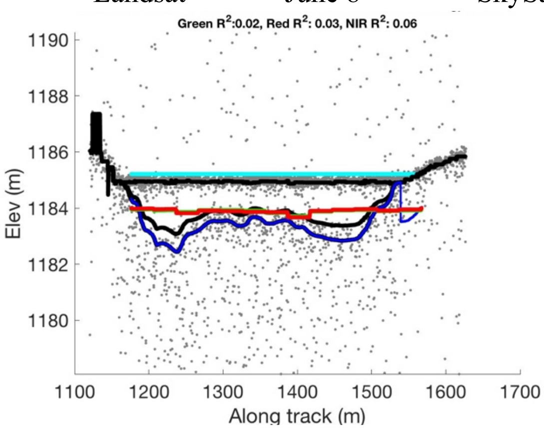

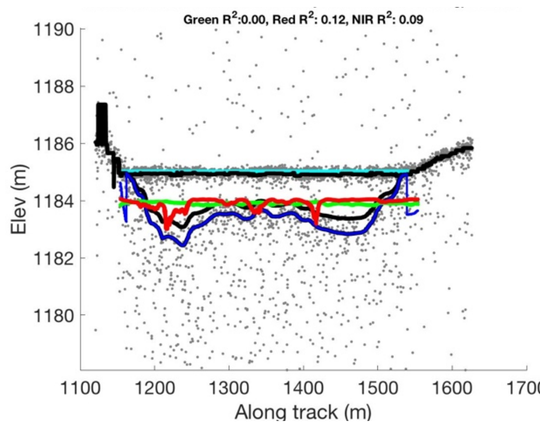

Lake 6

Landsat June 8th SkySat June 8th

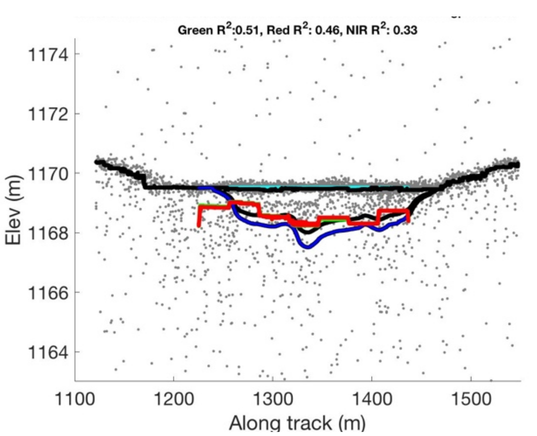

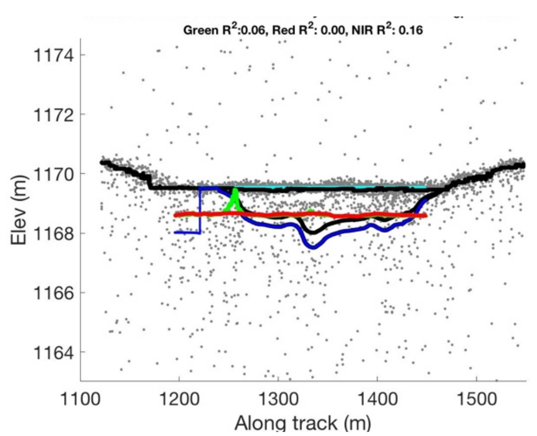

Lake 7

Landsat June 8th SkySat June 8th

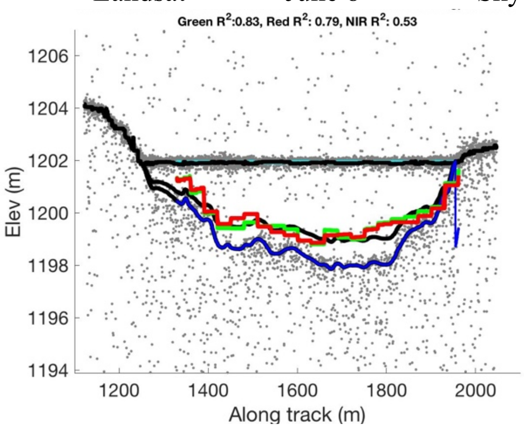

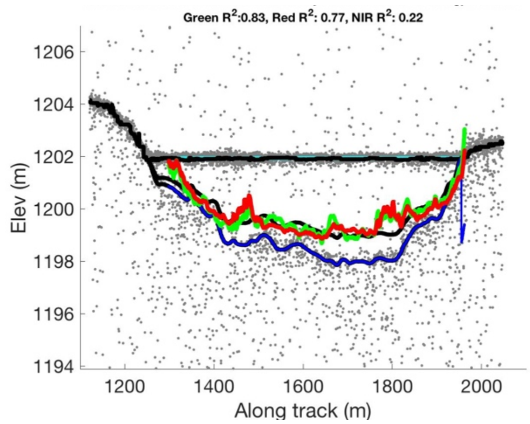

Lake 8

Landsat June 8th

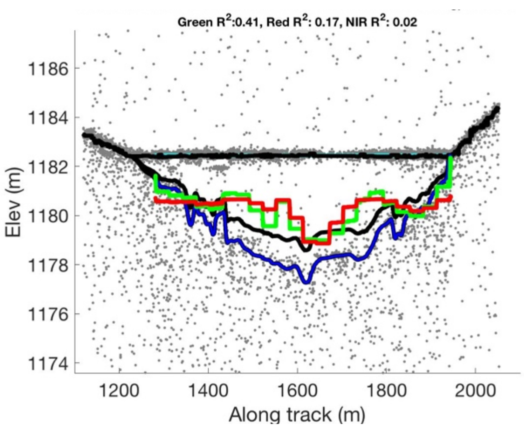

Lake 9

Landsat June 8th SkySat June 8th

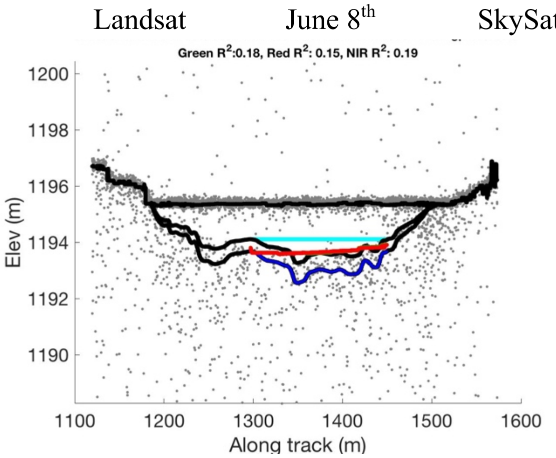

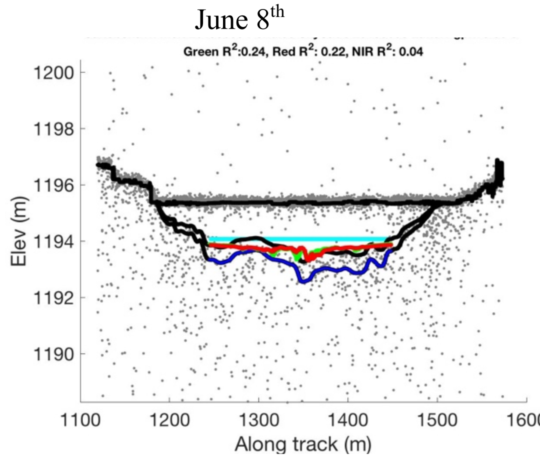

RGT 1108 June 9th, 2019

Lake 10

Landsat June 8th SkySat June 8th

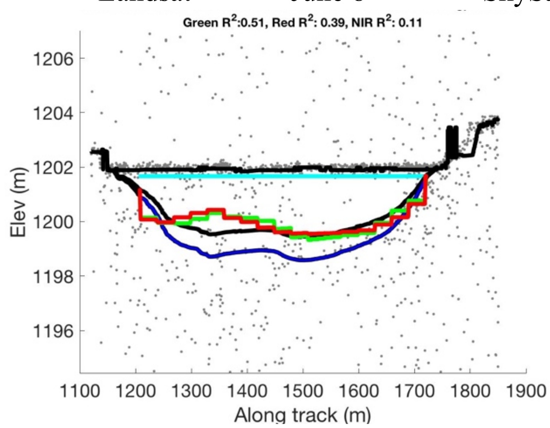

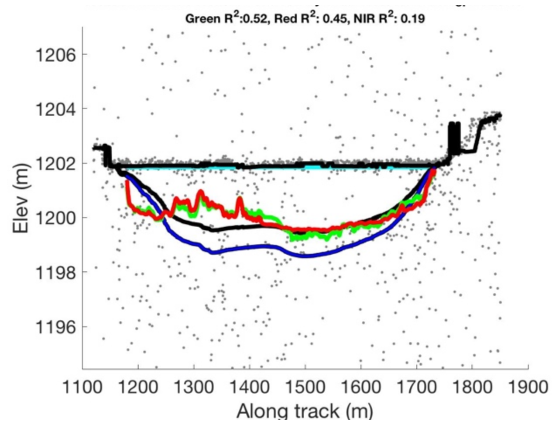

Lake 11

Landsat June 8th

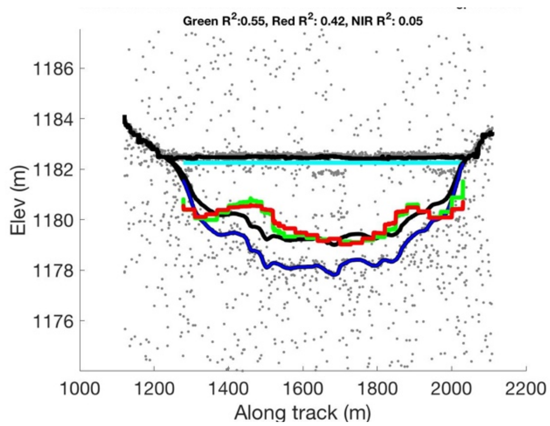

Lake 1

Landsat June 8th Sentinel-2 June 16th

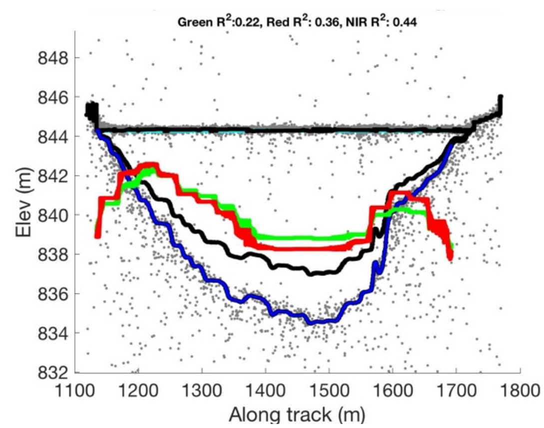

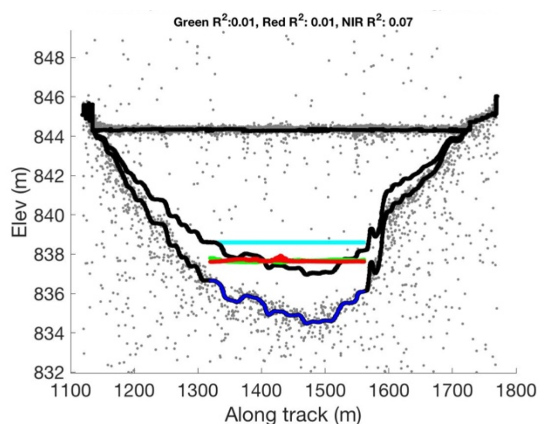

Lake 2

Sentinel-2 June 16th

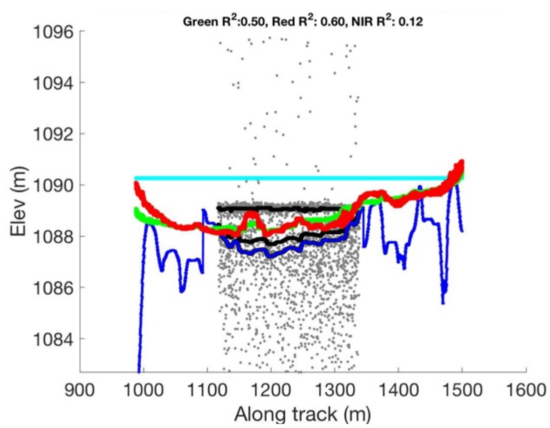

Lake 3

Landsat June 8th Landsat June 8th

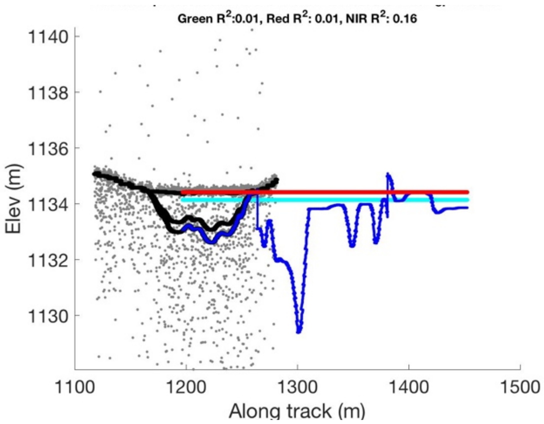

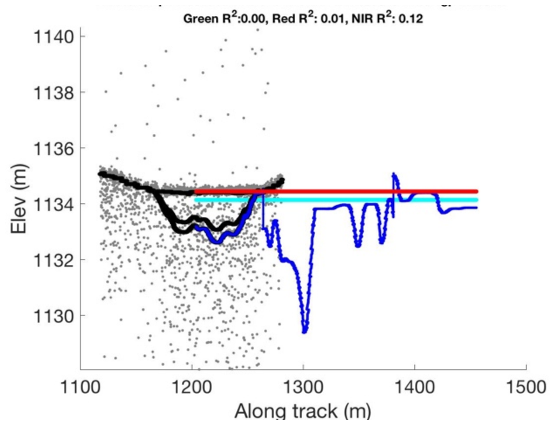

Sentinel June 16th

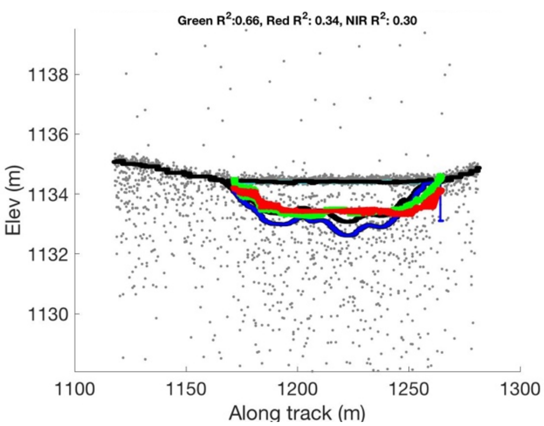

Lake 4

Sentinel-2 June 16th

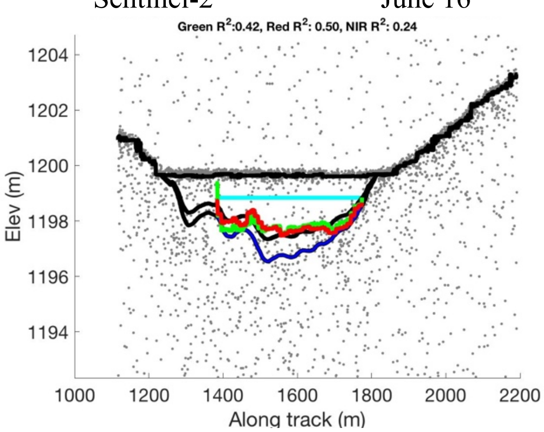

RGT 1169 June 13th, 2019

Lake 5

Landsat June 8th Sentinel-2 June 16th

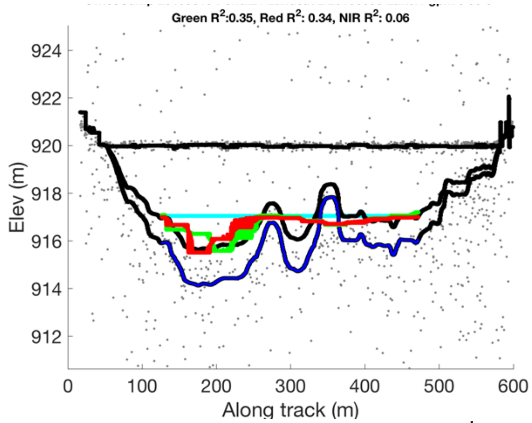

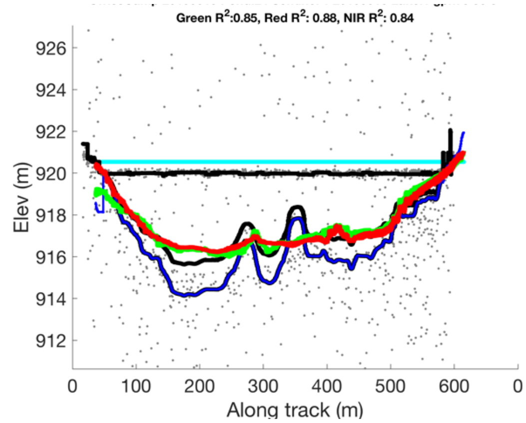

SkySat: June 14th

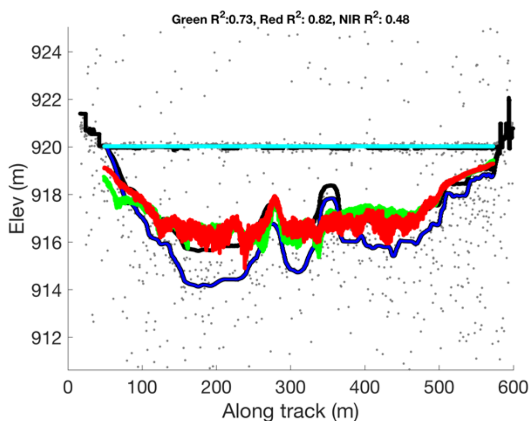

Lake 6

Landsat June 8th SkySat June 14th

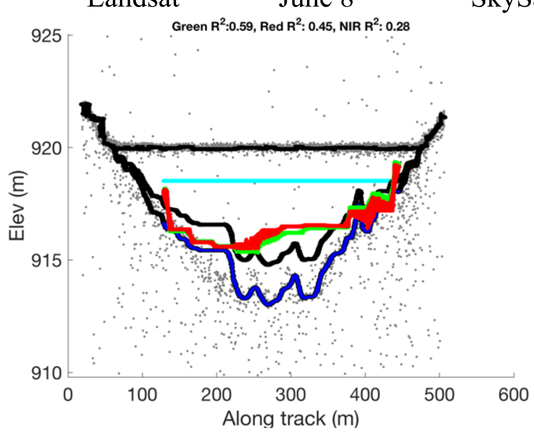

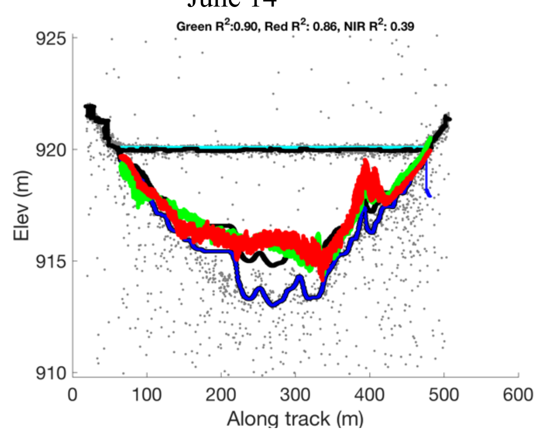

RGT 1169 June 13th, 2019

Lake 6 cont…

Sentinel-2 June 16th

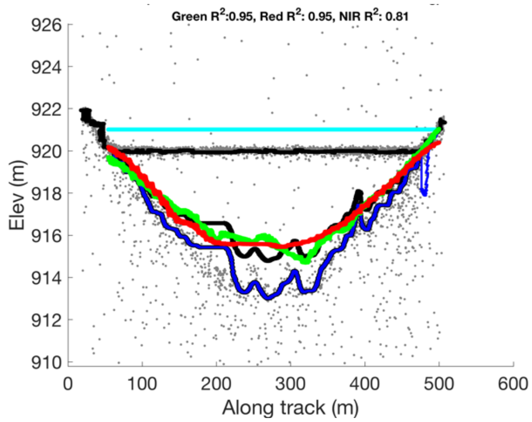

Lake 7

Sentinel-2 June 16th

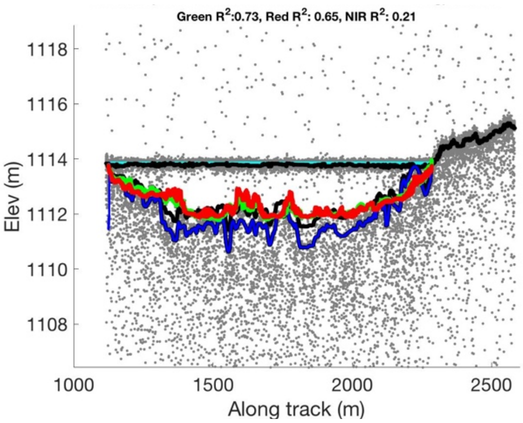

Lake 8

Landsat: June 8th

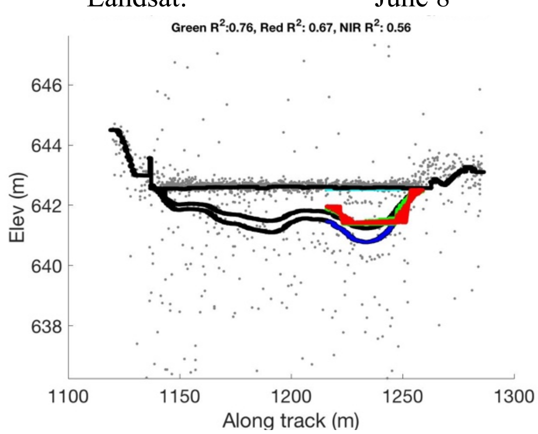

Sentinel-2 June 19th

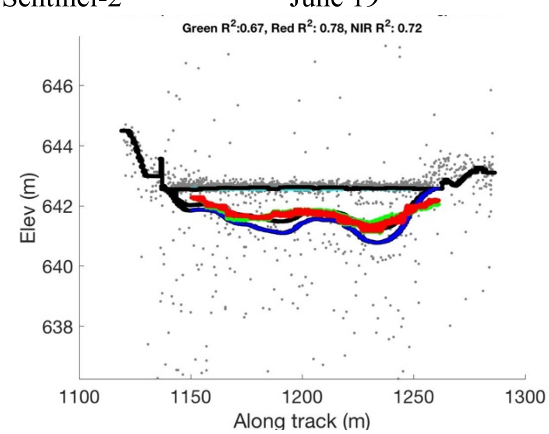

Lake 9

Sentinel-2 June 19th

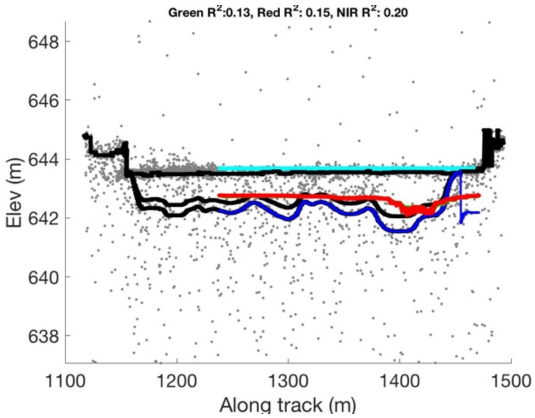

RGT 1222 June 17th, 2019

Lake 1

Landsat June 17th

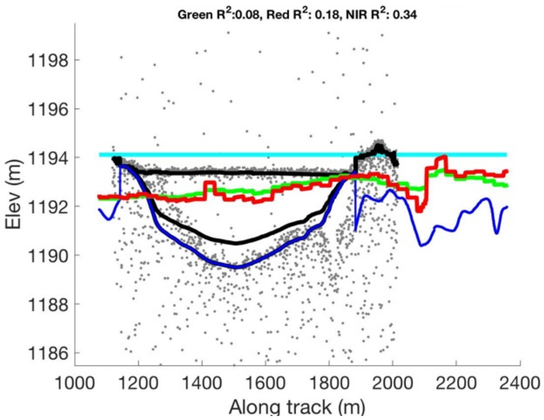

Lake 2

Landsat June 17th

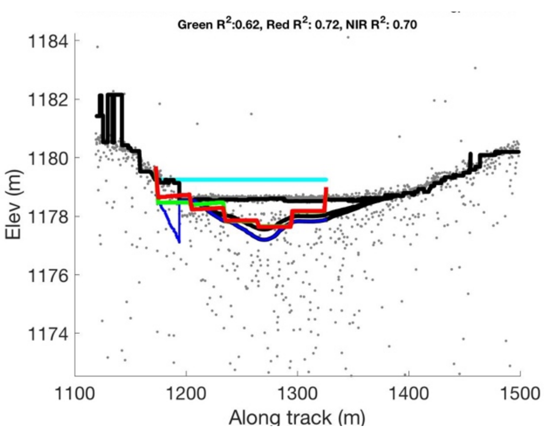

Lake 3

Landsat June 17th

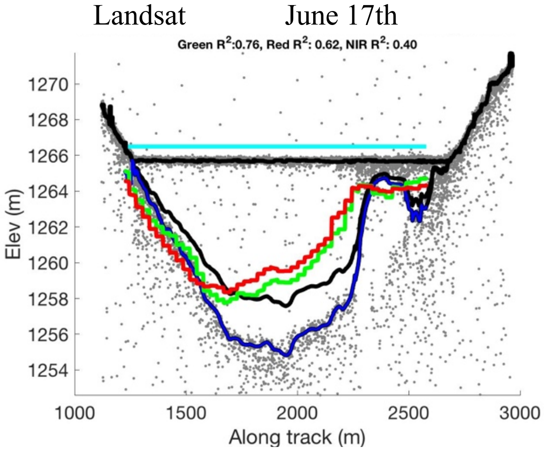

Lake 4

Landsat June 17th

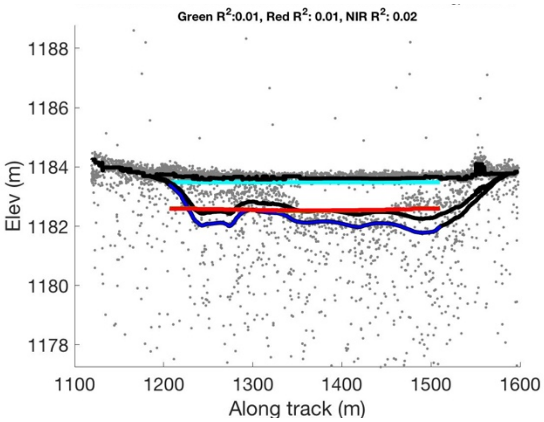

Lake 5:

Landsat June 17th

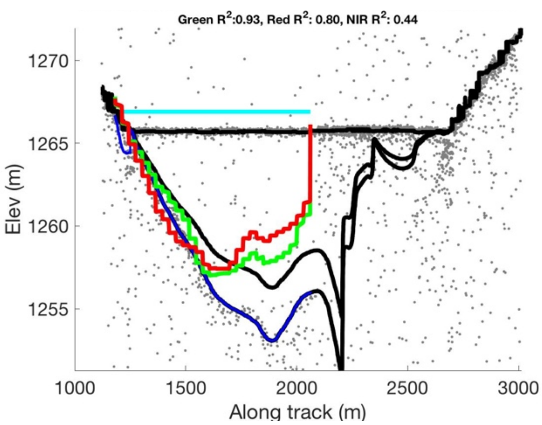

Lake 6

Landsat June 17th

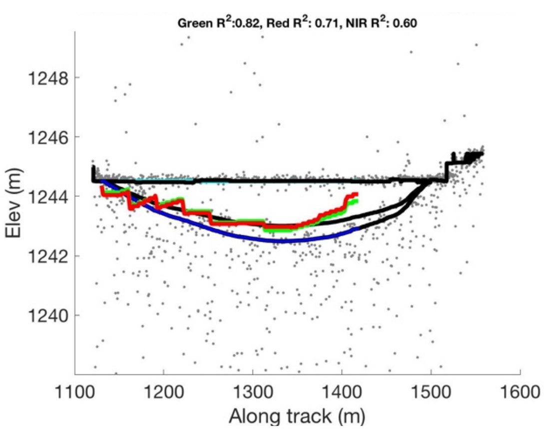

SkySat June 17th

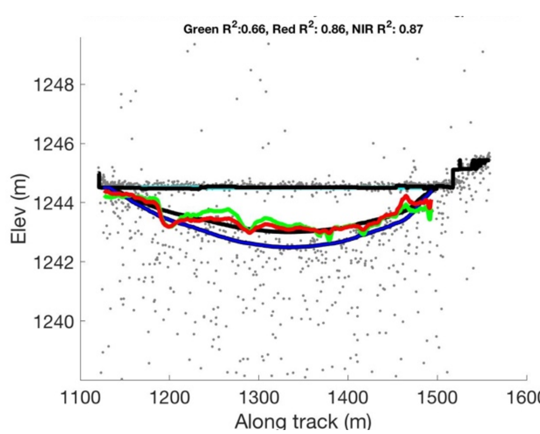

Lake 7:

Landsat June 17th

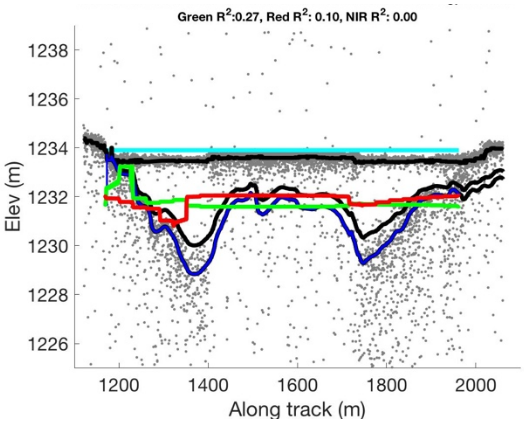

Lake 8:

Landsat June 17th

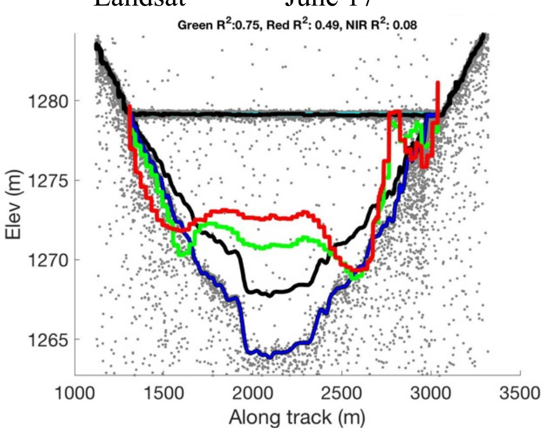

Lake 9:

Landsat June 17th

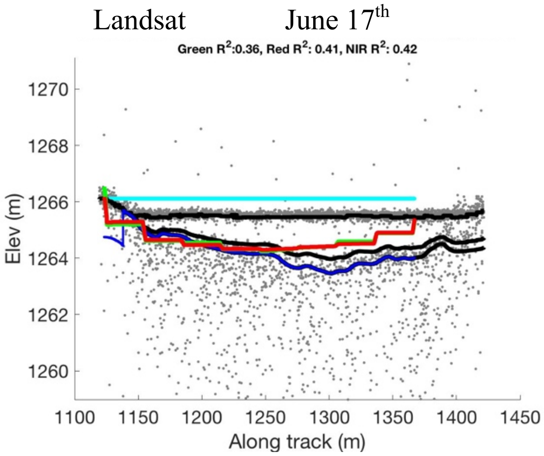

Lake 10

Landsat June 17th SkySat June 16th

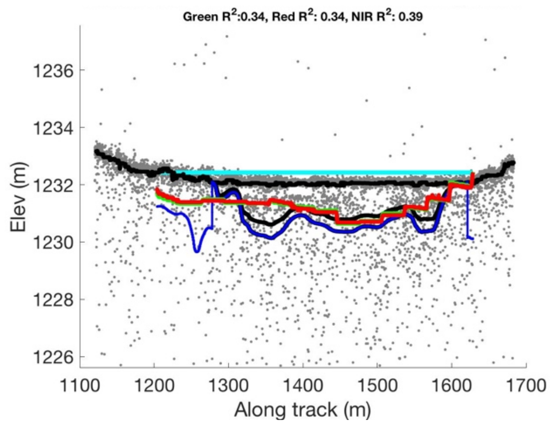

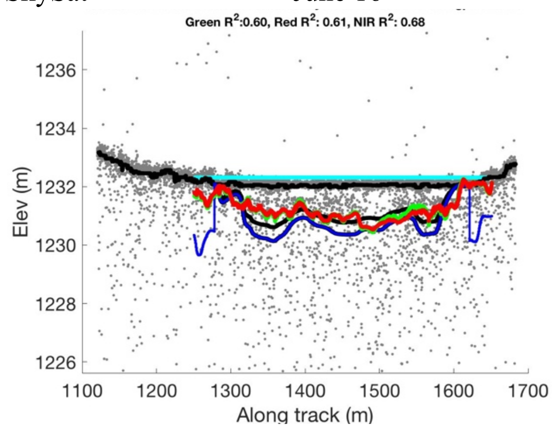

Lake 11

Landsat June 17th

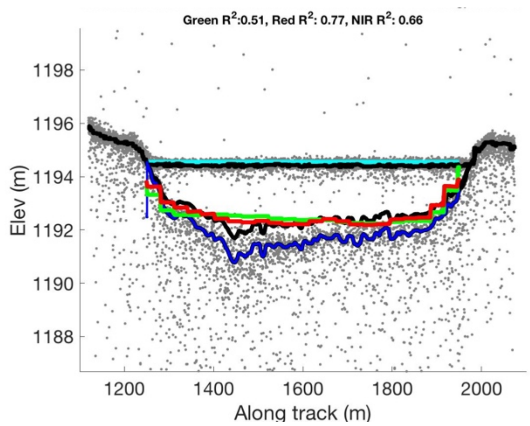

Lake 12

Landsat June 17th

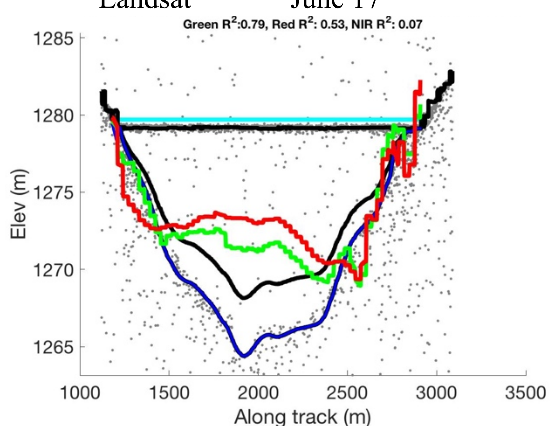

Lake 13

Landsat June 17th

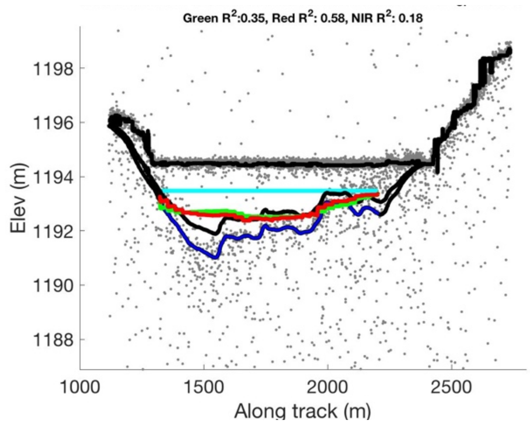

Lake 14

Landsat June 17th

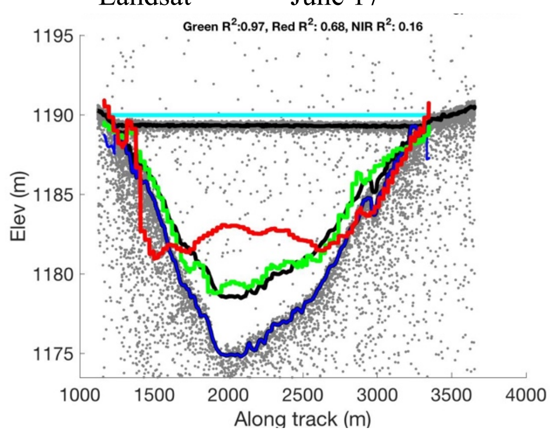

Lake 15

Landsat June 17th

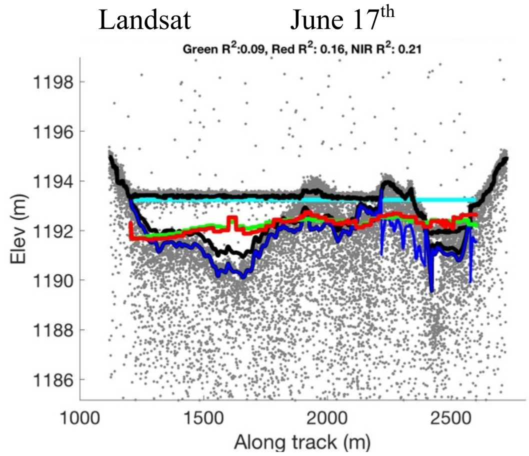

Lake 16

Landsat June 17th

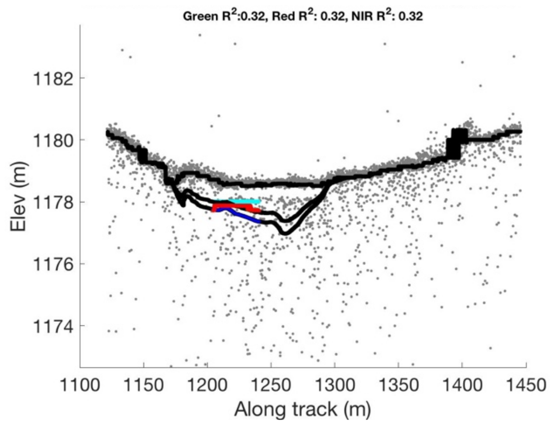

Lake 17

Landsat June 17th

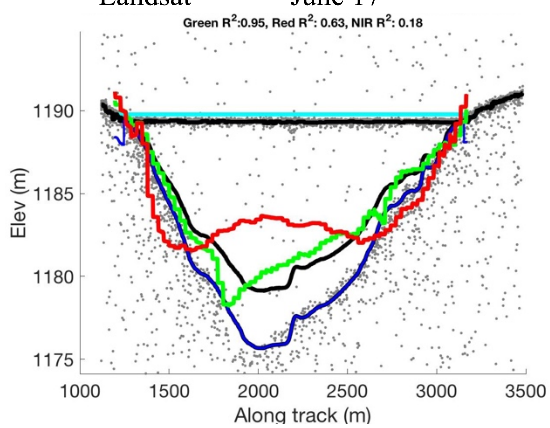

Lake 18

Sentinel-2 June 16th

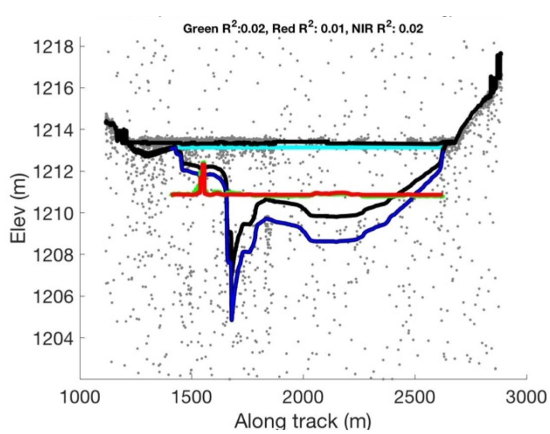

Lake 19

Sentinel-2 June 16th